Environmental Science & Technology

pubs.acs.org/est

Article

Bioinspired Solar-Driven Osmosis for Stable High Flux Desalination

Zihao Zhu,[§] Jianwei Xu,[§] Yingzong Liang,* Xianglong Luo,* Jianyong Chen, Zhi Yang, Jiacheng He, and Ying Chen

Cite This: *Environ. Sci. Technol.* 2024, 58, 3800−3811

Read Online

ACCESS | Metrics & More | Article Recommendations | Supporting Information

ABSTRACT: The growing global water crisis necessitates sustainable desalination solutions. Conventional desalination technologies predominantly confront environmental issues such as high emissions from fossil-fuel-driven processes and challenges in managing brine disposal during the operational stages, emphasizing the need for renewable and environmentally friendly alternatives. This study introduces and assesses a bioinspired, solar-driven osmosis desalination device emulating the natural processes of mangroves with effective contaminant rejection and notable productivity. The bioinspired solar-driven osmosis (BISO) device, integrating osmosis membranes, microporous absorbent paper, and nanoporous ceramic membranes, was evaluated under different conditions. We conducted experiments in both controlled and outdoor settings, simulating seawater with a 3.5 wt % NaCl solution. With a water yield of 1.51 kg m^{-2} h^{-1} under standard solar conditions (one sun), the BISO system maintained excellent salt removal and accumulation resistance after up to 8 h of experiments and demonstrated great cavitation resistance even at 58.14 °C. The outdoor test recorded a peak rate of 1.22 kg m^{-2} h^{-1} and collected 16.5 mL in 8 h, showing its practical application potential. These results highlight the BISO device's capability to address water scarcity using a sustainable approach, combining bioinspired design with solar power, presenting a viable pathway in renewable-energy-driven desalination technology.

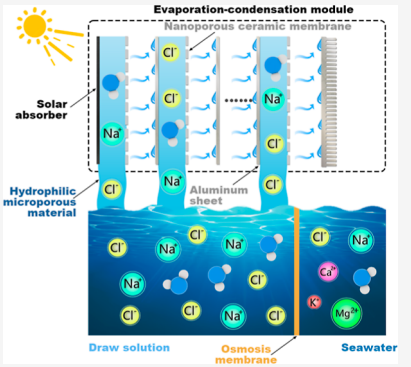

KEYWORDS: *capillary-pressure-driven osmosis, solar evaporation, seawater desalination, synthetic tree, multistage latent heat recovery*

1. INTRODUCTION

Water stress is a pressing issue faced by numerous countries and regions worldwide,[1] with 2.2−3.2 billion people residing in areas experiencing water scarcity.[2−4] In order to address this challenge, desalination has emerged as a feasible solution for augmenting water supplies.[5] However, mainstream desalination technologies, such as reverse osmosis and multieffect distillation, rely heavily on high-grade energy sources derived from fossil fuels and challenging brine treatment strategies,[6−9] contributing to environmental concerns.

In this context, recently, a lot of effort has been dedicated to the studies of renewable-energy-driven, robust, flexible desalination technologies able to operate even in emergency conditions.[10−13] Much attention has been paid to design novel techniques, with solar-powered distillation being particularly highlighted as a promising low-carbon solution of great potential.[14−16] Photovoltaic-driven reverse osmosis systems offer scalable, low-maintenance solutions for sustainable water production, especially in areas of high solar irradiance.[17,18] However, they depend highly on sustained high radiant flux sunlight and have high initial costs.[19,20] In contrast, solar thermal-driven desalination of seawater, characterized by its low cost, minimal maintenance, and compact design, offers advantages for deployment and widespread application in remote, water-scarce regions.[21−23] Furthermore, thermally driven desalination processes can employ multistage latent heat recovery strategies to enhance energy efficiency conveniently.[11,24,25] Conventional solar thermal distillation heats bulk water and results in a large amount of wasted thermal energy, hence solar-driven interfacial evaporation (SDIE) has been developed, with its feature of heat localization allowing the heat to be used more efficiently for evaporation.[26−28] However, before large-scale applications, salt accumulation in the SDIE system needs to be addressed[29,30] as salt crystals at the photothermal material or evaporation surface can obstruct the water supply channels and deteriorate the stable operation ability of the system.[31] Conventional flushing methods risk damaging the system's mechanical structure,[32] while some devices that can automatically clean at night often fail to maintain stable desalination throughout the day.[33] Moreover, the lack of experience in operating devices in complex environments and unclear understanding of the microscopic mechanisms have resulted in a significant gap between current solar-powered desalination technologies and practical applications.[34] In addition, complex manufacturing processes and material structures often increase the application

Received: October 28, 2023
Revised: January 25, 2024
Accepted: January 26, 2024
Published: February 13, 2024

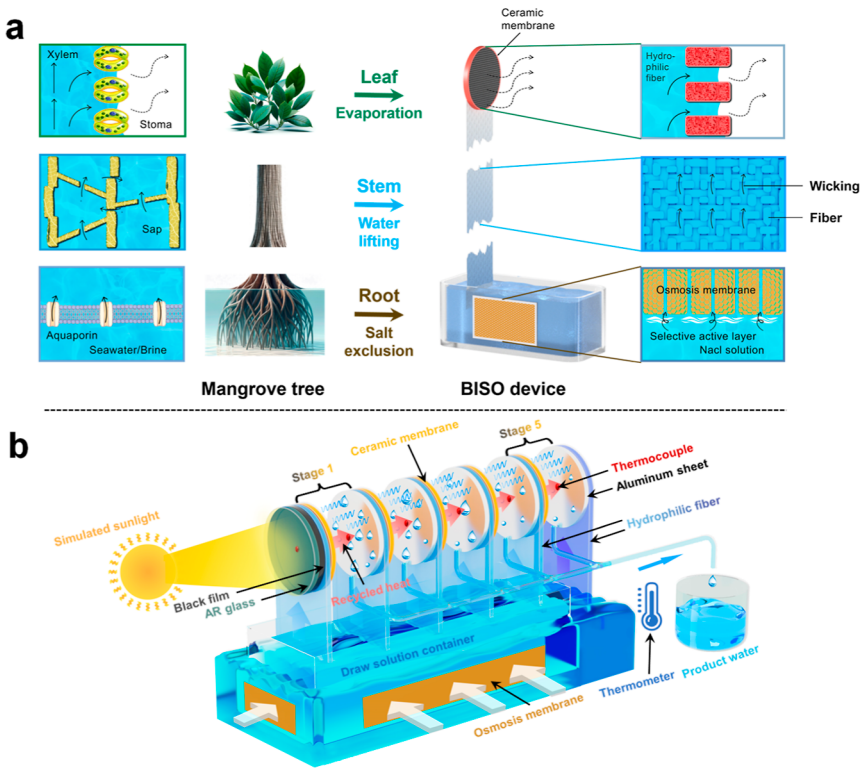

Figure 1. Illustration of a BISO device and design elements. (a) BISO device (right) parallels natural mangrove (left) water transport and salt filtration. (b) Schematic diagram of the BISO device's mechanism.

cost.[31] Nevertheless, improving the functional structure of solar-powered desalination such as SDIE to improve the stability of water production remains a favorable approach.[34] Besides controlling the impact of common salt in seawater on evaporation efficiency, SDIE also faces the challenge of effectively filtering and rejecting other inorganic salt particles, organic compounds, microorganisms, and bacteria.[35]

In view of the difficulties mentioned above that may be foreseeable and hinder the practical application of solar-powered desalination technology, approaches to address these issues include but are not limited to the development of composite materials and intricate structural designs.[36−39] A direct and efficient method for salt removal and contaminant retention is to utilize osmosis membranes with excellent rejection performance to separate seawater or brine from the evaporation surface. Wang et al.[13] successfully synthesized a device similar to a natural mangrove through bionics and realized a negative-pressure-driven desalination process. Their study confirms the applicability of cohesion−tension theory[40,41] in mangrove desalination and long-distance water transport and provides a new idea for engineering membrane separation. Due to their reliance solely on natural evaporation without introducing any additional heat source, the evaporation flux of the device is not very satisfactory (approximately 0.49 kg m^{-2} h^{-1}). Moreover, the water under high negative pressure, while being stretched, is in a metastable state,[42] making cavitation more likely to occur and leading to water column rupture,[43,44] impeding the water supply. In addition, considering the sensitivity of the cavitation behavior of metastable water to temperature,[45] it may limit the solar-driven evaporation temperature. In order to address the pressing need for convenient, stable, and off-grid solar-powered desalination solutions, it is essential to develop a universal desalination system that avoids the reliance on complex material processing and high costs. Moreover, such a system should demonstrate exceptional resistance to cavitation and exhibit efficient salt inhibition and removal capabilities.

In this study, we propose a modular bioinspired solar-driven osmosis (BISO) device that uses the draw solution to balance the osmotic pressure of seawater, which displays capabilities in terms of robust contaminant rejection (achieved primarily through the osmosis process), high productivity, and consistently producing clean water. This BISO device is characterized by five key features: an osmosis membrane effectively filtering salt and contaminants, a calibrated draw solution with osmotic pressure to facilitate high osmosis flux and ensure stable water production, a microporous absorbent paper that creates a capillary pressure that moves the draw solution from the osmosis membrane surface to the evaporation surface, a nanoporous superhydrophilic ceramic membrane that allows the draw solution to spread rapidly and evenly throughout the evaporation surface (and creates additional capillary pressure to enhance the osmosis process), and a multistage structure to recover rejected heat to improve solar-to-vapor efficiency. We demonstrate the BISO device's capacity to harness solar energy and significantly enhance water production, achieving a 1.51 kg m^{-2} h^{-1} flux under one sun (i.e., 1000 W m^{-2}) and a gained output ratio (GOR) greater than 1. Moreover, our system effectively mitigates challenges such as cavitation and drying out of the leaf, ensuring stable operation even at 58.14 °C (much higher than room temperature). This is because the draw solution facilitates the synchronization between evaporation and the osmosis flux rate and improves stability. The results suggest the synergetic effects achieved through the balance of osmotic pressure (difference) between the draw solution and feed

https://doi.org/10.1021/acs.est.3c08848
Environ. Sci. Technol. 2024, 58, 3800−3811

Table 1. Main Materials and Chemicals Used in the BISO Device and Experiments

materials/chemicals	purpose/application	supplier
NaCl (99.5% purity)	prepare the NaCl aqueous solution with a salinity of 35 g L^{-1} to simulate seawater and serve as the draw solution	Guangzhou Chemical Reagent Factory
$MgCl_2·6H_2O$ (98% purity), KCl (99.5% purity), $CaCl_2·2H_2O$ (98% purity)	prepare solution with varying solute (ion) compositions to evaluate the selective permeability performance of the osmosis membrane	
self-drying Teflon coating	applied on aluminum sheets to enhance their hydrophobic properties	Dongguan Fuwang New Material Technology Co., Ltd
antireflective (AR) glass	reduce reflection and thermal loss in solar absorbers and to provide protection	Schott Glaswerke AG
solar selective absorption coating (black film)	capture and convert solar energy	Jiangsu Hulse Coating Technology Co., LTD
nanoporous ceramic membrane	as evaporation surface for water and provide the auxiliary capillary force	Kunshan Tengerhui electronic Technology Co., LTD
osmosis membrane	reject solutes in seawater while allowing water to pass through	Guochu Technology (Xiamen) Co., Ltd
aluminum sheet	as a high thermal conductivity base material for coating with black film or Teflon	Guangdong Hongwang new material Technology Co., LTD
3D-printed resin frame	secure components in place and provide protection	Shenzhen future Workshop Technology Co., LTD
absorbent paper	provide the driving force for water transport and channels for water conveyance	Foshan Jiada nonwoven fabric Co., LTD
foam	provide insulation and reduce thermal loss from the device to the environment	Ningbo Hi-Tech Zone Weldon Home Technology Co., LTD

solution (e.g., seawater), capillary pressure generated by the microporous absorbent paper and the nanopore ceramic membrane, and the evaporation pressure difference between the evaporation layer and the environment.

2. WORKING PRINCIPLE

The detailed composition of the proposed BISO device for desalination is shown in Figure 1. The system utilizes capillary pressure in micropores of hydrophilic fibers, similar to the mechanism found in natural mangroves. In mangroves (illustrated in Figure 1a, left), the stomatal pores in the leaves generate capillary pressure that drives water up through xylem channels, while root cell membrane aquaporins facilitate salt removal from external liquids, such as seawater or brine. The negative pressure generated in the leaves and transmitted to the roots allows for overcoming the osmotic pressure of saline water. Trees in saline environments can adjust their sap osmotic pressure to reduce the required negative pressure. Correspondingly, the main components of the BISO device (depicted in Figure 1b, right) include a nanoporous ceramic membrane, a microporous absorbent paper, and a selective osmosis membrane, mirroring natural mangrove leaves, stems, and roots, respectively. The capillary pressures in the ceramic membrane and absorbent paper act synergistically to drive water from external liquid through the osmosis membrane. Capillary action creates negative pressure that moves the draw solution up to the evaporation surface (blue solid arrow in Figure 1a), thus eliminating the external pump. For desalination, the device must also overcome the osmotic pressure of seawater or salt water to drive water through the osmosis membrane. In the BISO device, the salinity of the draw solution can be adjusted to reduce the obstruction of water flow by seawater osmotic pressure. Water transport in natural mangrove xylem can be explained by the cohesion−tension theory: the tension created by negative pressure allows water to move upward against gravity and pressure drop, while cohesion ensures the continuity of the water column (see Supporting Information Note 2 for details). The cohesion−tension theory also explains the flow of water in the absorbent paper of the BISO device. The draw solution in the BISO device can balance the osmotic pressure of the feed fluid; hence, the absolute value of the negative pressure could be lower. This ensures adequate osmotic flow and mitigates cavitation risks (see Supporting Information Note 3 for details). Moreover, the nanopores of the ceramic membrane provide additional capillary pressure, which can assist the absorbent paper (capillary action of the micropores) in facilitating the flow of the draw solution. In addition, vertically aligned fiber channels could facilitate the solute back into the draw solution container. Coated with a black film, the first-stage aluminum sheet converts solar flux into thermal energy, heating the draw solution (Figure 1b). The black film provides a photothermal conversion efficiency of approximately 93%, enabling effective solar-to-thermal energy conversion that heats the draw solution in absorbent paper. This heated solution flows through the ceramic membrane and evaporates at its air−liquid interface. In the BISO device's operation, the selective permeability of the osmosis membrane effectively blocks salts and impurities from seawater, allowing only pure water to enter the draw solution container. The evaporation process occurring at the surface of the ceramic membrane involves the separation of water from the solutes (i.e., NaCl) in the draw solution. Capillary action continuously draws the solutions upward to compensate for the outgoing vaporized water, thereby sustaining evaporation. The latent heat released during this process energizes subsequent evaporation stages. The final stage features an aluminum sheet connected to a beaker filled with seawater via absorbent paper, ensuring that it remains close to ambient temperature. Vapor pressure differentials between the ceramic membrane (evaporator) and the aluminum plate (condenser) induce a mass transfer of water vapor. Then, water vapor condensed on the condenser is gravity-collected. The latent heat thus released powers the subsequent stage, establishing an energy recycling mechanism to improve the device's energy efficiency. In order to improve the water production in the final stage, an additional hydrophilic fiber sheet is placed at the tail of its aluminum sheet to enhance heat dissipation and vapor condensation. Each evaporation−condensation stage is divided by two aluminum sheets and reinforced by a resin frame to ensure the stability of the structure. The aluminum's high thermal conductivity (a typical value of 237 W m^{-1} K^{-1}) allows for

https://doi.org/10.1021/acs.est.3c08848
Environ. Sci. Technol. 2024, 58, 3800−3811

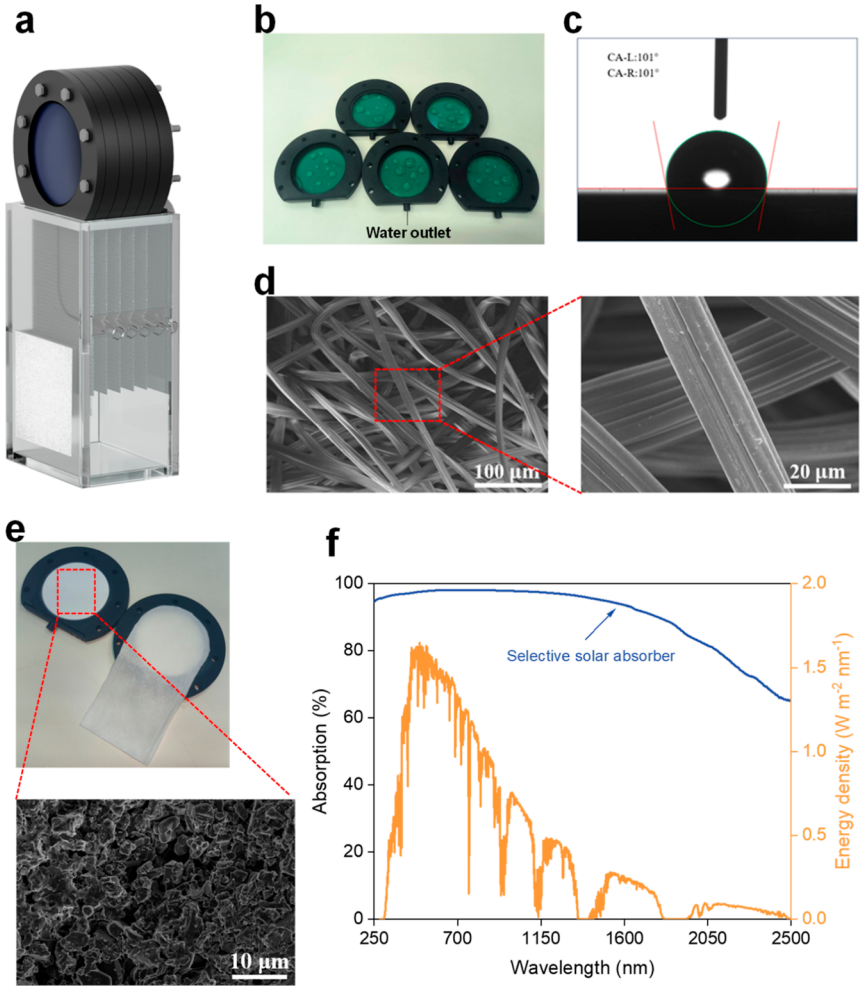

Figure 2. Design and characterization of the five-stage evaporation−condensation BISO device. (a) 3D simulated schematic of the BISO device. (b) Optical image of the condenser. Aluminum sheet with a Teflon coating (Supporting Information Note 6). (c) Teflon coating's contact angle. (d) SEM image of the microporous absorbent paper. (e) Optical and SEM images of the nanoporous ceramic membrane. (f) Absorption spectrum of the solar absorber.

effective interstage heat recovery. The resin frame is enclosed with an insulated foam cover to minimize heat loss to the environment. It is sealed with poly(tetrafluoroethylene (PTFE) tape to reduce evaporation of the draw solution to the environment. Lastly, the BISO system uses a selective osmosis membrane to eliminate heat-sensitive and heavy-metal contaminants, thus ensuring water purity and long-term device stability. Unlike conventional solar stills, the BISO is characterized by a multistage evaporation−condensation design that avoids light-blocking problems caused by condensation droplets, effectively increasing the mass transfer driving force to increase the vapor yield.

3. MATERIALS AND METHODS

3.1. Materials and Chemicals. Various chemicals and materials are used in the construction and operation of the BISO device, as listed in Table 1. All of these chemicals are analytical-reagent-grade and can be used directly without further purification.

3.2. Detailed Design and Preparation Statement. Figure 2a outlines the assembly structure of the multistage BISO device, with further details elaborated in Supporting Information Note 4. The device is built from six 3D-printed resin frames secured with stainless steel fasteners. The initial frame's front interior is braced with a 6 cm diameter, 1 mm thick AR glass to shield the heat absorber and mitigate thermal loss. A spectrally selective solar absorber (black film, 5 cm in diameter) is embedded in its rear interior. Subsequent resin frames feature consistent internal components: each incorporates a 5 cm diameter, 2 mm thick nanoporous ceramic membrane at the front, serving as the evaporator. A 6 mm air gap, greater than the typical droplet sizes on the condenser, ensures pure condensed water collection without contact with the evaporator. The first layer of absorbent paper is sandwiched between the solar absorber and the evaporator of the first stage. Subsequent layers of absorbent paper are interposed between the condenser of each stage and the following stage's evaporator. This configuration facilitates effective latent heat recovery during each stage's heat transfer, occurring from the aluminum sheet, through the absorbent paper, and ultimately to the ceramic membrane. In order to monitor thermal dynamics, six thermocouples are affixed to every evaporation−condensation stage, while an industrial-grade thermometer captures ambient temperature readings. Each condenser employs a 0.5 mm thick aluminum sheet installed in the rear of the respective stage. A 1 μm thick Teflon layer is applied to the aluminum sheet to encourage droplet formation and prevent spillage. The process for

https://doi.org/10.1021/acs.est.3c08848
Environ. Sci. Technol. 2024, 58, 3800−3811

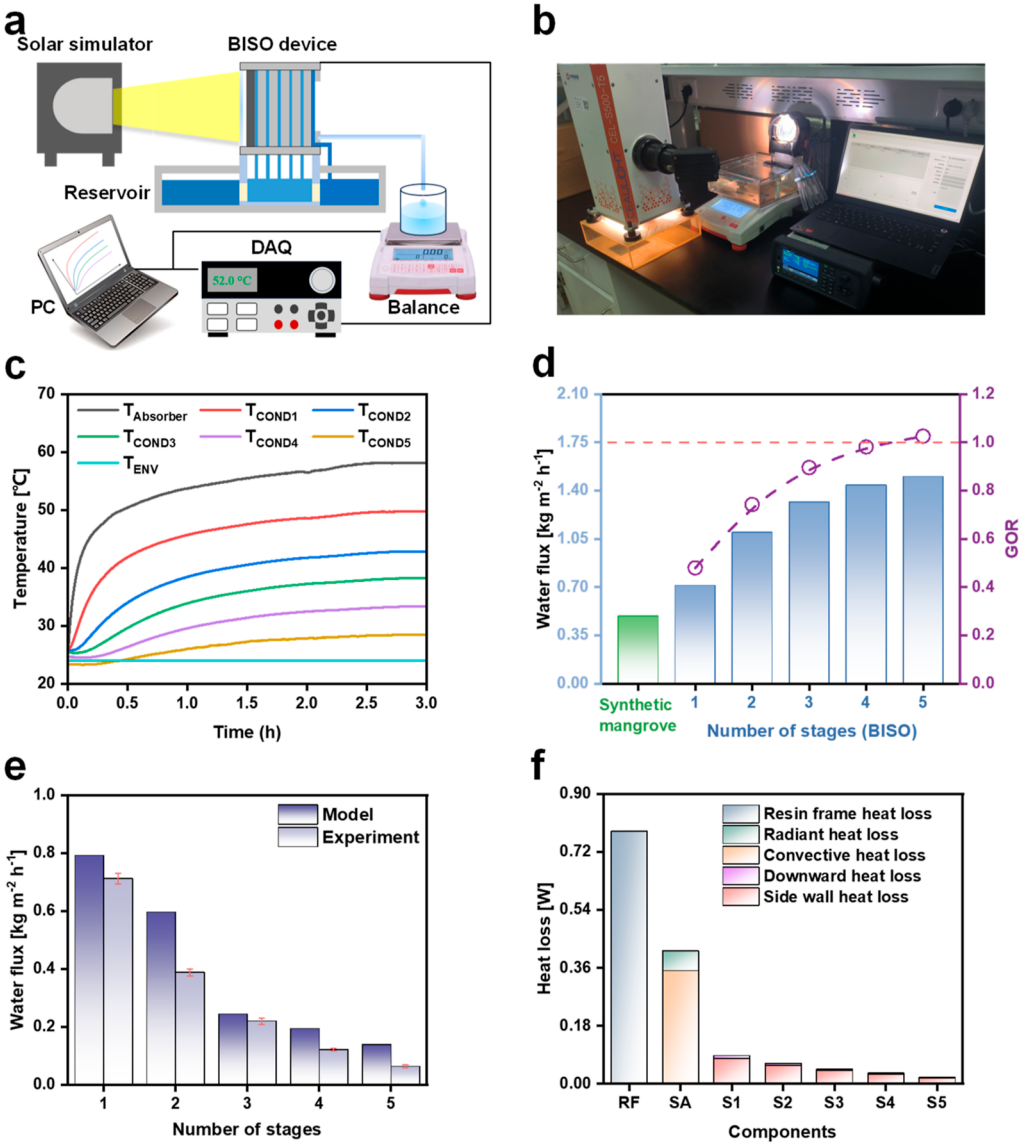

Figure 3. Operating performance of a five-stage evaporation−condensation BISO device. (a) Schematic representation of the experimental setup. (b) Detailed photograph showcasing the elaborate details of the fully assembled BISO device. (c) Diagram illustrating the gradual temperature progression at stages for 3 h. $T_{Absorber}$ refers to the solar absorber's temperature, while T_{COND1} through T_{COND5} represent the temperatures recorded at the condenser surfaces from stages one to five. T_{ENV} denotes the room temperature. (d) Performance of the BISO device. (e) Comparison of the water yield calculated by the theoretical model with the experimental water yield. (f) Breakdown of the heat loss of the evaporation−condensation module. RF and SA represent the resin frame and solar energy absorber, respectively, and S1−S5 represent the evaporation−condensation stages from the first to the fifth stage, respectively.

recovering the latent heat from condensation is facilitated through a pathway where thermal energy is conducted from the condenser via the absorbent paper to the evaporator in the subsequent stage. The PTFE tape lining on each frame ensured the sealing of the evaporator. The final stage's external absorbent paper is attached to the condenser with PTFE tape. Details of the design and assembly of the BISO device, such as the placement and angling of the condensed water drainage hole, are discussed in Supporting Information Note 4. The annular resin frame design positions the water outlet at its lowest point to facilitate gravity-driven water collection. Water flows to the inner surface of the frame, converges at the annular outlet, and is channeled for collection. An acrylic five-sided box, with dimensions of 8 × 6 × 13 cm^3, serves as the draw solution container. Two rectangular holes, one located in the lower front and the other in the lower back of the container, are cut out, and each of these holes is sealed with a piece of osmotic membrane. The multistage evaporation−condensation module is placed above the container, with the former's absorbent paper extending into the container. A 5 × 1 cm^2 slit is located on the container's exterior, 8 cm above the bottom, to accommodate tubing from the resin frames.

3.3. Characterization. The hydrophobicity observation and contact angle measurement of the Teflon surface on the aluminum surface are shown in Figure 2b,c, respectively, with the Teflon coating characterized by a contact angle of 101°, underlining its hydrophobic nature. As illustrated in Figure 2d, the scanning electron microscopy (SEM) image of the absorbent paper reveals its microporous structure with intertwined hydrophilic fibers creating numerous pores ranging in diameter from 10 to 100 μm, forming multiple channels for effective water transport. This structure generates a robust

https://doi.org/10.1021/acs.est.3c08848
Environ. Sci. Technol. 2024, 58, 3800−3811

capillary effect, facilitating the upward movement of the draw solution. Tests confirmed that water rises to 135 mm in 6 min (approximately 3.75×10^{-5} m s^{-1}; see Supporting Information Note 5). Moreover, Figure 2e displays the nanopore size distribution of the ceramic membrane, which provides an additional negative-pressure driving force for the osmosis process. Figure 2f presents the absorption spectrum of the solar absorber from 300 to 2500 nm, as recorded by a UV−vis−near-infrared (NIR) spectrophotometer. This spectrally selective absorber exhibits a high solar absorption rate of about 93% and a thermal emission rate of 7% in the 0.3 to 1.5 μm wavelength range, confirming the solar absorber's effectiveness in harnessing solar energy and high efficiency for solar-driven evaporation. Detailed characterization results can be found in Supporting Information Note 7.

3.4. Experimental Procedure. This section outlines the methodology employed in both laboratory-controlled and outdoor experimental setups. The draw solution's concentration is prepared to equal that of simulated seawater.

3.4.1. Indoor Experiments. An acrylic box measuring 8 cm in height and serving as the seawater basin was filled with simulated seawater. The box featured a 7 × 9 cm^2 opening designed to accommodate the BISO device's draw solution container. A five-stage evaporation−condensation module was positioned above the opening of the draw solution container, and the absorbent paper was immersed below the level of the draw solution container. The final stage's condenser was externally wrapped in absorbent paper (heat sink), and the tail end of the paper was submerged in a beaker to dissipate the condensation heat and lower the condenser's temperature. Owing to the resin material's relatively low thermal resistance, characterized by a thermal conductivity of approximately 0.2 W m^{-1} K^{-1}, we have implemented a strategy to reduce thermal losses. This involves insulating the resin frames with 1 cm thick foam, boasting a significantly lower thermal conductivity of 0.04 W m^{-1} K^{-1}, enhancing the system's overall thermal efficiency. The condensate was collected in 1 cm diameter centrifuge tubes. A solar simulator (CEL-S500-T5, CEAULIGHT) supplied a consistent 1000 W m^{-2} solar flux gauged by a photometer (CEL-NP2000-2A, CEAULIGHT). A data acquisition device (DAQ970A, KEYSIGHT) monitored temperatures from six type-K thermocouples. The seawater basin was placed on top of a high-precision balance (NX3000, YOUHENG), enabling real-time mass loss tracking. This balance was interfaced with a PC through a serial port cable (RS232, UGREEN), and the data was captured at 10 s intervals. Each experiment was replicated thrice, replacing solutions after each run.

3.4.2. Outdoor Experiments. Conducted in Guangzhou, China, on August 5, 2023, the BISO device's outdoor evaluation was performed from 9:00 to 17:00. The evaporation−condensation module was oriented toward the sun at a 30° angle for optimal solar exposure. A photometer (CEL-NP2000-2A, CEAULIGHT), aligned at a similar angle, recorded the fluctuating solar flux levels. An industrial thermometer measured the ambient conditions. The produced condensate was flowed into a 30 mL graduated cylinder.

4. RESULTS AND DISCUSSION

4.1. Indoor Performance Characterization. Figure 3a displays the experimental arrangement for the BISO system, first assessed within a controlled laboratory setting. The solar simulator delivers a solar flux of 1000 W m^{-2}, enabling operation of the BISO device. In order to capture real-time thermal data, six thermocouples were deployed: one for monitoring the solar absorber's surface temperature and five for each condensation stage. The electronic balance is used to weigh the collected condensate. The data is acquired and analyzed by a data acquisition device connected to the PC. Figure 3b presents a high-resolution photograph of the actual BISO system. It should be noted that the balance is displayed here to record the osmotic mass loss of the seawater basin. Temperature readings were concurrently logged on a computer, and the instantaneous temperature profiles for individual measurement points are illustrated in Figure 3c. Enabled by the AR-coated glass and foam insulation, the solar absorber's surface attained an effective operating temperature of approximately 50 °C within 30 min, peaking later at 58.14 °C. Subsequent stages stabilized sequentially, and the system stabilized in roughly 2.8 h, after which the surface temperatures exhibited minimal fluctuations, denoting a stable operating state. Notably, the outflow of condensed water from the first stage was observed approximately 12 min after the start of the experiment. Nearly 2.5 h into the experiment, the condensate began to flow out of the final stage. Uniform thermal resistance across stages resulted in an approximately linear decrease in the temperature gradient at each stage. While the seawater in the beaker absorbs the heat of the end condenser, the steady-state temperature of this heat sink (∼25.8 °C) is slightly elevated compared to the ambient temperature (∼24 °C) due to the thermal resistance of the absorbing paper. After a steady state is reached, the electronic balance begins to record the production of collected condensate and the mass loss of the seawater basin. Notably, the final-stage condenser maintains a temperature close to the environmental baseline, differing by 3 °C. Figure 3d plots the water flux of each evaporation−condensation stage. In stabilized conditions, the total water flux of the five-stage assembly was measured at 1.51 kg m^{-2} L^{-1}. It is worth noting that the total water flux is tested by the mass change (or mass flow) of the condensate collected in the centrifugal tube measured by an electronic balance. When the equipment is in stable operation, the initial mass readings of each centrifuge tube are obtained, setting a baseline. The BISO device then continues to operate for 1 h, and a subsequent measurement round rerecords the tubes' masses again. The mass variance of each tube over this hour indicates the hourly water accumulation per stage. Each stage's condensation flux is established by dividing the hourly water accumulation by the corresponding condensation area. The sum of these flux values at all stages gives the total water flux of the system. Due to thermal energy losses and diminishing energy grades, the single stage's vapor mass flux gradually declined with an increasing number of stages. Consequently, the first two stages were the most productive, contributing over 73% to the total water flux.

The gain output ratio (GOR) is used as an indicator to evaluate the efficiency of water production

$$\mathrm{GOR} = \frac{\dot{m} \cdot h_{ev}}{q_{solar} \cdot A}$$

where $\dot{m}$ represents the total mass flow rate of water in kg s^{-1}; h_{ev} is the enthalpy of water vaporization in J kg^{-1} $°C^{-1}$; q_{solar} is the solar radiation flux in W m^{-1}; and A denotes the effective area of the heat-absorbing surface in m^{-2}. We formulated a comprehensive mathematical model to analyze the interplay between heat and mass transfer within the system, focusing on

https://doi.org/10.1021/acs.est.3c08848
Environ. Sci. Technol. 2024, 58, 3800−3811

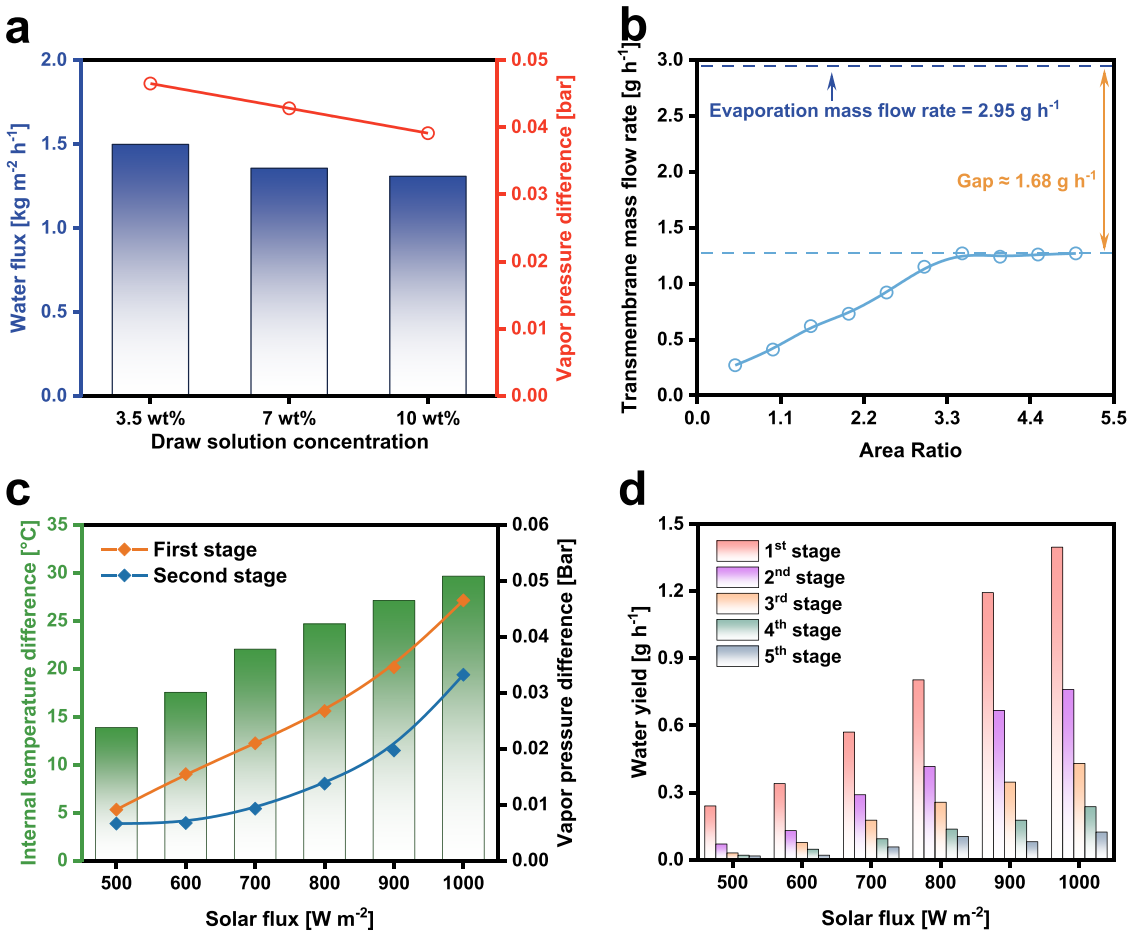

Figure 4. Influence of key parameters on the water production performance of a five-stage evaporation−condensation BISO device. (a) Increase in the concentration of the draw solution decreases water flux. (b) Relationship between the area ratio and transmembrane mass flow rate. (c) Influence of different solar fluxes on the internal temperature difference. (d) Water production at each stage under different solar fluxes.

steady-state conditions. As illustrated in Figure 3d, the model indicates that the steady-state GOR of the BISO device exceeds unity (to reach 102.6%). Maintaining a stable vapor mass flux at each evaporation−condensation stage highlights the device's proficiency in latent heat recuperation, transcending the theoretical limitations imposed on single-stage systems (100%). Despite observing a sequential decrement in water flux across each stage relative to that of its predecessor, the first stage condensation flux of the BISO device notably surpasses the evaporation flux of the synthetic mangrove, as illustrated by the green bar in Figure 3d. This outcome underscores the BISO device's passive yet efficient water production capability, especially considering the stable operation and excellent osmosis desalination (see Subsection 3.2). In terms of water production, overall, the theoretical model predicts yields higher than those of the experimental data (Figure 3e). The total water collection rate is 76.62%. This difference is attributed to tiny droplet adherence to the condensation surface or the internal recess of the resin frame and vapor leakage. Enhancing the condenser and resin channel surfaces' hydrophobicity and sealing conditions can optimize the production efficiency. Furthermore, a discrepancy is observed between the theoretical and experimental water fluxes in the second stage, with the theoretical values being higher. In contrast, the third stage demonstrates a closer alignment between theoretical and experimental fluxes. This variation could be attributed to manual errors in thermocouple measurements, potentially arising from factors such as the positioning of the thermocouples, their installation methods, and unintentional thermal leakage stemming from the wiring configurations. These factors impact the accuracy of temperature readings. Such a deviation could result in underestimating the second stage's condensation temperature and the third stage's evaporation temperature, thus leading to anomalies in theoretical fluxes in these two stages compared to those in the others. When the solar flux is 1000 W m^{-2}, the actual solar energy received by the device is estimated to be 1.81 W, considering the solar absorber's small area. As shown in Figure 3f, convective and radiative losses from the solar energy absorber are calculated as 0.35 and 0.06 W, respectively. The lateral surfaces of the device contribute to 15.45% of the total heat loss to the environment (0.22 W), while the downward losses could be negligible (approximately 1.59%). The heat loss mainly comes from the resin frame's heat dissipation to the environment, about 0.78 W, accounting for more than 54.38% of the total heat loss.

Furthermore, we investigated the impact of key experimental parameters—such as the draw solution concentration, the area ratio (defined as the osmosis membrane area divided by a single ceramic membrane sheet area), and the solar flux—on the water production capabilities of the five-stage evaporation−condensation BISO device. As illustrated in Figure 4a, a rise in the salt concentration diminishes the vapor pressure at the evaporation surface, undermining the mass transfer drive

https://doi.org/10.1021/acs.est.3c08848
Environ. Sci. Technol. 2024, 58, 3800−3811

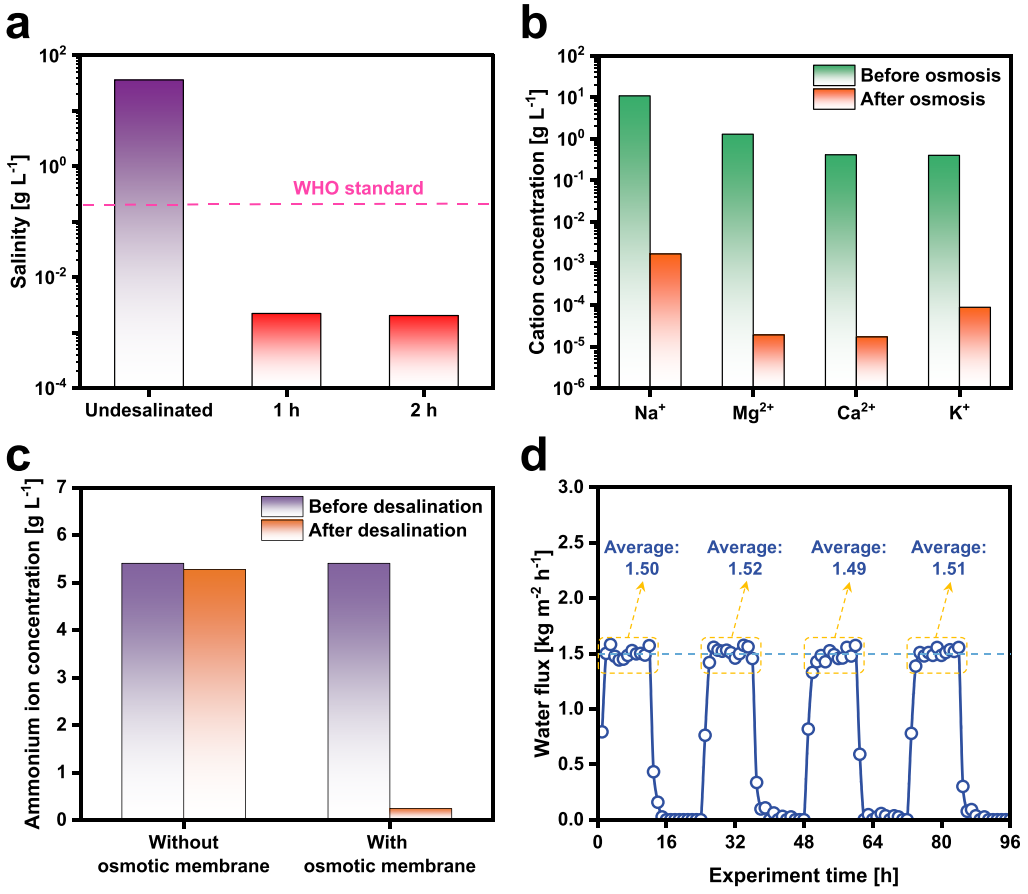

Figure 5. Analysis of the BISO device's desalination efficacy and stability. (a) Comparative salinity pre- and post-desalination. (b) Selectivity of the osmosis membrane. (c) Performance test of the BISO device for removal of volatile components. (d) Device stability across multiple experiments.

between the evaporation and condensation surfaces. The red circle in the diagram shows the difference in vapor pressure between the evaporation and condensation surfaces of the first stage. The theoretical model, under a solar flux of 1000 W m^{-2}, exhibits a narrowing in the vapor pressure differential between the first stage's evaporation and condensation surfaces—from 9.17 to 8.39 kPa—as the draw solution concentration increases from 3.5 to 10 wt %. This led to a 13% reduction in water flux, dropping from 1.51 to 1.31 kg m^{-2} h^{-1}. Figure 4b reveals the impact of varying area ratios (ranging from 0.5 to 5) on the transmembrane mass flow rate. A noteworthy observation was that raising the area ratio from 0.5 to 3.5 substantially increased the transmembrane mass flow rate from 0.27 to 1.27 g h^{-1}. Moreover, a discrepancy can be observed between the osmotic and evaporation mass flows, where the latter remained relatively steady at 2.95 g h^{-1}. A small area ratio hinders the appropriate replenishment of fluids, restricting the water flow from seawater to the drawing solution. Nevertheless, enlarging the area ratio shows a ceiling of the transmembrane mass flux. This phenomenon hints at a delayed replenishment of the evaporated liquid from the seawater source, changing the system's state during operation with a continuous uptick in the draw solution concentration. Figure 4c showcases the dynamics of the internal temperature differential under diverse solar flux conditions. A trend was observed where the internal temperature gap at the evaporator escalated from 14 to 30 °C with the solar flux increasing from 500 to 1000 W m^{-2}. However, an interesting aspect was the decelerating pace of the growth of the temperature differential with higher solar flux. This is due to the increase in the surface temperature of the solar absorber. On the one hand, the evaporation flux would increase and take away more heat from the absorber; on the other hand, it would also increase the convection and radiation loss to the surrounding environment alongside heat escape at each stage's resin frame and sidewall. The solar flux demonstrates a significant role in determining water yield; elevating the solar flux 2-fold from 500 to 1000 W m^{-2} boosted the water production rate by 6.8 times (from 0.38 to 2.95 g h^{-1}), illustrated in Figure 4d. Notably, under each solar flux analyzed, the first two stages constituted the most water production, contributing over 70% to the total output across all five stages.

4.2. Salt Rejection Performance and Stability. We used a NaCl solution with a 36 g L^{-1} concentration as a feed solution to evaluate the BISO device's desalination performance. Figure 5a demonstrates that, within stable operation, the salinity of the collected water decreased to between 2.0×10^{-3} and 2.2×10^{-3} g L^{-1}, a reduction of 4 orders of magnitude. This outcome significantly surpasses the global drinking water standard of 0.2 g L^{-1} established by the WHO (represented by the pink dashed line). The BISO device demonstrated remarkable resistance to the primary challenge of salt accumulation, which is a critical problem in conventional solar evaporation systems. This resistance is attributed to the osmosis membrane's selectivity that effectively prevents the salt transfer from the seawater basin to the draw solution container, thereby reducing the potential for contaminants to reach the evaporation layer. Furthermore, the absorbent paper's vertical

https://doi.org/10.1021/acs.est.3c08848
Environ. Sci. Technol. 2024, 58, 3800−3811

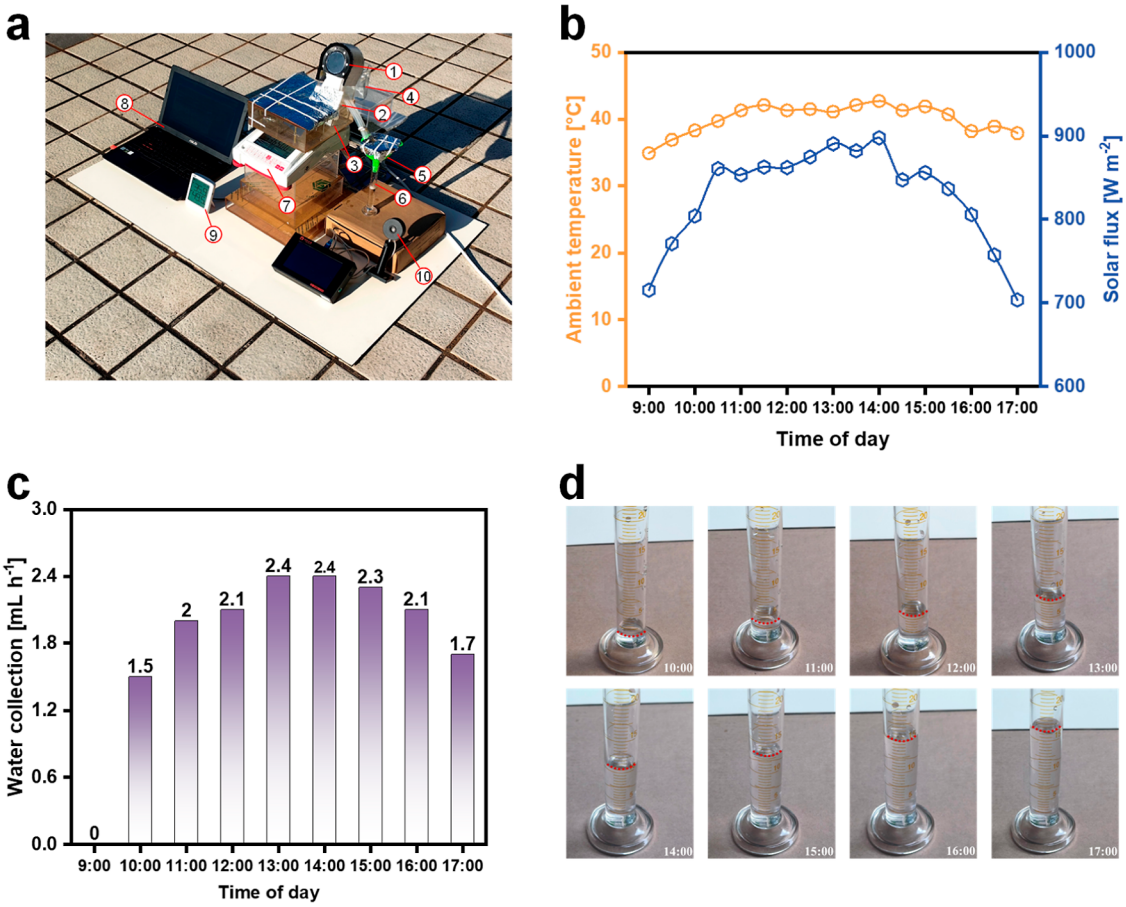

Figure 6. Outdoor testing of the BISO systems on August 5, 2023. (a) Experimental setup. The test bench was equipped with a variety of apparatuses, including (1) a five-stage evaporation−condensation module inclined at a 30° angle, (2) a draw solution container, (3) a seawater basin, (4) a beaker with submerged absorbent paper, (5) a funnel, (6) a 30 mL graduated cylinder, (7) a balance, (8) a computer, (9) an industrial-grade thermometer, and (10) a photometer set at a 30° tilt. (b) Outdoor tests record real-time ambient temperature and solar flux fluctuations. (c) Water yield of the system at different periods. (d) Optical image of the water level of condensate in the graduated cylinder changing over time.

positioning encourages salt's downward diffusion, improving the device's salt resistance. The detailed salt removal effect of the BISO device is described in Supporting Information Note 8. As Figure 5b shows, we undertook tests to assess the desalination capabilities of the osmosis membrane. The results of the cation concentration in simulation seawater before and after osmosis showed that the contents of common cations in seawater (including Na^+, Mg^{2+}, Ca^{2+}, and K^+) were significantly reduced by over 99.9%, corresponding to a decrease of 4−5 orders of magnitude, thus demonstrating the superior selectivity of the membrane. Figure 5c shows the BISO device's dual desalination mechanism of evaporation and osmosis to remove volatile contaminants. We used an ammonium carbonate solution with a concentration of 14.4 g L^{-1} as the feed liquid (ammonium ion concentration of 5.4 g L^{-1}) to test the removal rate of volatile substances. In the absence of osmosis membranes, only evaporative desalination is relied on, and heat-sensitive volatile substances pollute the collected water (such as ammonium carbonate decomposition to NH_3 and CO_2). Therefore, the ammonium ion concentration in the condensate is basically unchanged, which is only reduced by 2.41% to 5.27 g L^{-1} compared to that in the feed liquid. After the osmosis membrane is used, the ammonium ion concentration of the condensate can be reduced by more than 95.52%, and its concentration is only 0.24 g L^{-1}. This high contaminant rejection rate ensures sustained and stable water production, around 1.50 kg m^{-2} h^{-1}, over several cycles, as indicated in Figure 5d, throughout a 96 h experimental period. Consequently, the data suggest that the BISO device can operate effectively for extended periods, demonstrating a high resistance to cavitation at temperatures exceeding the ambient temperature and a reliable performance over repeated operation. During the operation of the device, there is a negligible elevation in the concentration of solutes on the osmosis membrane's outer surface. It is attributable that the diffusive water uptake of the BISO device is comparable to the natural seawater flow, and the ambient seawater movement continuously thins the concentrated saline water surrounding the osmosis membrane. This effective dilution could minimize brine discharge,[46] addressing a significant environmental challenge in conventional desalination processes. In addition, the water production of the BISO device across various inclination angles was assessed (detailed in Supporting Information Note 9). We also rigorously investigated the device's resistance to biofouling under actual seawater conditions, as elaborated in Supporting Information Note 10.

4.3. Outdoor Operation Experiment. We set up an experiment in Guangzhou, China, on August 5, 2023, to evaluate the device's outdoor performance. The tests were conducted on the outdoor platform on the second floor of the laboratory building at the Guangdong University of Technology Guangzhou Higher Education Mega Center Campus. The

https://doi.org/10.1021/acs.est.3c08848
Environ. Sci. Technol. 2024, 58, 3800−3811

weather was cloudy, with temperatures ranging from 26 to 35 °C, and the relative humidity was 69%. As shown in Figure 6a, the BISO system was mounted on a wooden board. The five-stage evaporation−condensing unit is inserted into the upper opening of the draw solution pool at a 30° angle, and the draw solution container is inserted into the seawater basin. An industrial thermometer was employed to monitor the ambient temperatures, while a specially aligned photometer recorded the solar flux descending on the absorber. The condensate from each stage was collected in a graduated cylinder, and a balance connected to a computer tracked the mass loss from the seawater basin. This experiment started at 9:00 and ended at 17:00 local time, offering a demonstration of the BISO device's performance throughout the day. Figure 6b outlines the variations in ambient temperature and solar irradiance that day, indicating a peak ambient temperature of 40 °C and an average solar irradiance of 0.83 sun. The solar flux ranged between roughly 700 and 900 W m^{-2}. Specifically, the ambient temperature at 9:00 is 34.9 °C, and the solar flux is 715 W m^{-2}; between 12:30 and 14:00, the highest solar flux is 875−898 W m^{-2}, and the corresponding ambient temperature fluctuates between 41.3 and 42.7 °C; at 17:00, the solar flux was down to 704 W m^{-2}. The solar flux is crucial in determining the absorber's temperature and the system's water yield. As illustrated in Figure 6c, the system showed robustness despite periodic fluctuations due to changing weather conditions and the sun's position, initiating water droplet formation 30 min after activation. From 1.5 mL h^{-1} at 10:00 to a peak of 2.4 mL h^{-1} (1.22 kg m^{-2} h^{-1}) at 13:00−14:00, water production slowly decreases to 1.7 mL h^{-1} at 17:00 as the solar flux decreases. Figure 6d shows the cumulative water collected over the 8 h. The condensate was gathered in a 30 mL graduated cylinder with the water level changes recorded using a camera. The amount of condensate collected at 17:00 is 16.5 mL, thereby underscoring the device's potential for practical application.

5. IMPLICATIONS

This study introduces an innovative BISO system. Simulating mangroves in nature, it achieves effective seawater desalination through the synergy of a series of components. The core components of the BISO system include an osmosis membrane, an absorbent solution with adjustable concentration, a microporous absorbent paper, a nanoporous ceramic membrane, and a multistage evaporation−condensation module designed to recover the latent heat of condensation and improve the efficiency of solar energy to vapor. The system's working principle depends on several key physical processes and interactions between components. First, the absorbent paper attracts the draw solution to the evaporation surface through a capillary action. The superhydrophilic ceramic membrane allows the draw solution to spread rapidly and evenly across the evaporation surface, creating additional capillary pressure to enhance the osmotic process. In addition, the osmosis membrane has excellent salt resistance properties that inhibit the entry of salts and contaminants into the draw solution. It is also important to note that the presence of the draw solution balances the osmotic pressure of seawater to facilitate the flow of water from seawater to the evaporation surface.

In the experiment, the BISO system demonstrated a water yield of 1.51 kg m^{-2} h^{-1} under one solar condition, maintaining a continuous and stable freshwater yield and stability against cavitation (up to 58.14 °C) during 96 h of operational testing. In the outdoor testing, the system achieved a peak water yield of 1.22 kg m^{-2} h^{-1}. This feasibility benchmark shows the system's performance under actual application in environmental conditions. The results also show that the BISO device can desalinate 36 g L^{-1} seawater to 2.0 × 10^{-3} to 2.2 × 10^{-3} g L^{-1}, which is significantly lower than the WHO's maximum permissible salt concentration in drinking water. It highlights the potential of BISO to provide safe, drinkable water. In addition, due to the dual desalination mechanism of evaporation and osmosis, the BISO equipment has shown excellent performance in treating solutions containing volatile pollutants, which can also significantly reduce the concentration of harmful substances. This is important for the protection of human health and the environment.

Overall, this study reveals the effectiveness of the BISO system under experimental conditions and points to its potential value in practical industrial applications. Through an in-depth understanding of the working principle and detailed analysis of experimental data, this paper emphasizes the importance of this novel desalination technology in increasing water production, optimizing energy use, and ensuring water quality safety, providing a new direction for current desalination practices.

■ ASSOCIATED CONTENT

Supporting Information

The Supporting Information is available free of charge at https://pubs.acs.org/doi/10.1021/acs.est.3c08848.

Detailed heat and mass transfer model and parameters; heat and mass transfer schematic in the BISO device; brief introduction to cohesion−tension theory and cavitation in the metastable liquid; detailed design and structure of the BISO device; water transport performance test of the absorbent paper; preparation of hydrophobic coating on the aluminum sheet; key component characterization; salt rejection tests; influence of inclination angle; and biofouling assessment (PDF)

■ AUTHOR INFORMATION

Corresponding Authors

Yingzong Liang − *School of Materials and Energy, Guangdong University of Technology, Guangzhou 510006, China; Guangdong Province Key Laboratory on Functional Soft Matter, Guangdong University of Technology, Guangzhou 510006, China;* orcid.org/0000-0003-1943-8750; Email: yliang@gdut.edu.cn

Xianglong Luo − *School of Materials and Energy, Guangdong University of Technology, Guangzhou 510006, China; Guangdong Province Key Laboratory on Functional Soft Matter, Guangdong University of Technology, Guangzhou 510006, China*; Email: lxl-dte@gdut.edu.cn

Authors

Zihao Zhu − *School of Materials and Energy, Guangdong University of Technology, Guangzhou 510006, China*

Jianwei Xu − *School of Materials and Energy, Guangdong University of Technology, Guangzhou 510006, China*

Jianyong Chen − *School of Materials and Energy, Guangdong University of Technology, Guangzhou 510006, China;*

https://doi.org/10.1021/acs.est.3c08848
Environ. Sci. Technol. 2024, 58, 3800−3811

Guangdong Province Key Laboratory on Functional Soft Matter, Guangdong University of Technology, Guangzhou 510006, China

Zhi Yang − *School of Materials and Energy, Guangdong University of Technology, Guangzhou 510006, China; Guangdong Province Key Laboratory on Functional Soft Matter, Guangdong University of Technology, Guangzhou 510006, China*

Jiacheng He − *School of Materials and Energy, Guangdong University of Technology, Guangzhou 510006, China; Guangdong Province Key Laboratory on Functional Soft Matter, Guangdong University of Technology, Guangzhou 510006, China*

Ying Chen − *School of Materials and Energy, Guangdong University of Technology, Guangzhou 510006, China; Guangdong Province Key Laboratory on Functional Soft Matter, Guangdong University of Technology, Guangzhou 510006, China*

Complete contact information is available at: https://pubs.acs.org/10.1021/acs.est.3c08848

Author Contributions

[§]Z.Z. and J.X. contributed equally to this paper.

Notes

The authors declare no competing financial interest.

■ ACKNOWLEDGMENTS

The authors acknowledge the financial support from the National Natural Science Foundation of China (52376004).

■ REFERENCES

(1) Scanlon, B. R.; Fakhreddine, S.; Rateb, A.; de Graaf, I.; Famiglietti, J.; Gleeson, T.; Grafton, R. Q.; Jobbagy, E.; Kebede, S.; Kolusu, S. R.; Konikow, L. F.; Long, D.; Mekonnen, M.; Schmied, H. M.; Mukherjee, A.; MacDonald, A.; Reedy, R. C.; Shamsudduha, M.; Simmons, C. T.; Sun, A.; Taylor, R. G.; Villholth, K. G.; Vörösmarty, C. J.; Zheng, C. Global water resources and the role of groundwater in a resilient water future. *Nat. Rev. Earth Environ.* **2023**, *4* (2), 87−101.

(2) UN World Water Development Report. Partnerships and cooperation for water supply and sanitation. 2023, https://www.unesco.org/reports/wwdr/2023/en/water-supply-and-sanitation (accessed April 2023).

(3) UN. Water- at the center of the climate crisis. 2023, https://www.un.org/en/climatechange/science/climate-issues/water (accessed July 2023).

(4) UN. Ensure Availability and Sustainable Management of Water and Sanitation for All; Department of Economic and Social Affairs, 2021, https://unstats.un.org/sdgs/report/2022/Goal-06/?_gl=1*1sfu09u*_ga*MTMxMDUyNzEzMC4xNjg5NTA5NjEz*_ga_TK9BQL5X7Z*MTY4OTUwOTYxMi4xLjEuMTY4OTUxMDI5Ny4wLjAuMA (Accessed on August 21, 2023).

(5) Lu, X.; Elimelech, M. Fabrication of desalination membranes by interfacial polymerization: history, current efforts, and future directions. *Chem. Soc. Rev.* **2021**, *50* (11), 6290−6307.

(6) Shahzad, M. W.; Burhan, M.; Ng, K. C. A standard primary energy approach for comparing desalination processes. *npj Clean Water* **2019**, *2* (1), 1.

(7) Al-Obaidi, M. A.; Filippini, G.; Manenti, F.; Mujtaba, I. M. Cost evaluation and optimisation of hybrid multi effect distillation and reverse osmosis system for seawater desalination. *Desalination* **2019**, *456*, 136−149.

(8) Liu, S.; Wang, Z.; Han, M.; Zhang, J. Embodied water consumption between typical desalination projects: Reverse osmosis versus low-temperature multi-effect distillation. *J. Clean. Prod.* **2021**, *295*, 126340.

(9) Giwa, A.; Dufour, V.; Al Marzooqi, F.; Al Kaabi, M.; Hasan, S. Brine management methods: Recent innovations and current status. *Desalination* **2017**, *407*, 1−23.

(10) Zhang, C.; Liang, H. Q.; Xu, Z. K.; Wang, Z. Harnessing solar-driven photothermal effect toward the water-energy nexus. *Adv. Sci.* **2019**, *6* (18), 1900883.

(11) Morciano, M.; Fasano, M.; Boriskina, S. V.; Chiavazzo, E.; Asinari, P. Solar passive distiller with high productivity and Marangoni effect-driven salt rejection. *Energy Environ. Sci.* **2020**, *13* (10), 3646−3655.

(12) Sheng, M.; Yang, Y.; Bin, X.; Zhao, S.; Pan, C.; Nawaz, F.; Que, W. Recent advanced self-propelling salt-blocking technologies for passive solar-driven interfacial evaporation desalination systems. *Nano Energy* **2021**, *89*, 106468.

(13) Wang, Y.; Lee, J.; Werber, J. R.; Elimelech, M. Capillary-driven desalination in a synthetic mangrove. *Sci. Adv.* **2020**, *6* (8), No. eaax5253.

(14) Wang, Z.; Horseman, T.; Straub, A. P.; Yip, N. Y.; Li, D.; Elimelech, M.; Lin, S. Pathways and challenges for efficient solar-thermal desalination. *Sci. Adv.* **2019**, *5* (7), No. eaax0763.

(15) Ahmed, F. E.; Hashaikeh, R.; Hilal, N. Solar powered desalination-Technology, energy and future outlook. *Desalination* **2019**, *453*, 54−76.

(16) Xu, N.; Li, J.; Finnerty, C.; Song, Y.; Zhou, L.; Zhu, B.; Wang, P.; Mi, B.; Zhu, J. Going beyond efficiency for solar evaporation. *Nat. Water* **2023**, *1* (6), 494−501.

(17) Mito, M. T.; Ma, X.; Albuflasa, H.; Davies, P. A. Reverse osmosis (RO) membrane desalination driven by wind and solar photovoltaic (PV) energy: State of the art and challenges for large-scale implementation. *Renew. Sustain. Energy Rev.* **2019**, *112*, 669−685.

(18) Helal, A. M.; Al-Malek, S. A.; Al-Katheeri, E. S. Economic feasibility of alternative designs of a PV-RO desalination unit for remote areas in the United Arab Emirates. *Desalination* **2008**, *221* (1−3), 1−16.

(19) Bilton, A. M.; Kelley, L. C.; Dubowsky, S. Photovoltaic reverse osmosis-Feasibility and a pathway to develop technology. *Desalination Water Treat.* **2011**, *31*, 24−34.

(20) Rahimi, B.; Shirvani, H.; Alamolhoda, A. A.; Farhadi, F.; Karimi, M. A feasibility study of solar-powered reverse osmosis processes. *Desalination* **2021**, *500*, 114885.

(21) Chamsa-ard, W.; Fawcett, D.; Fung, C. C.; Poinern, G. Solar thermal energy stills for desalination: a review of designs, operational parameters and material advances. *J. Energy Power Eng.* **2020**, *2* (4), 2004018.

(22) Bamasag, A.; Almatrafi, E.; Alqahtani, T.; Phelan, P.; Ullah, M.; Mustakeem, M.; Obaid, M.; Ghaffour, N. Recent advances and future prospects in direct solar desalination systems using membrane distillation technology. *J. Clean. Prod.* **2023**, *385*, 135737.

(23) Chiavazzo, E. Critical aspects to enable viable solar-driven evaporative technologies for water treatment. *Nat. Commun.* **2022**, *13* (1), 5813.

(24) Alberghini, M.; Morciano, M.; Fasano, M.; Bertiglia, F.; Fernicola, V.; Asinari, P.; Chiavazzo, E. Multistage and passive cooling process driven by salinity difference. *Sci. Adv.* **2020**, *6* (11), No. eaax5015.

(25) Wang, W.; Shi, Y.; Zhang, C.; Hong, S.; Shi, L.; Chang, J.; Li, R.; Jin, Y.; Ong, C.; Zhuo, S.; Wang, P. Simultaneous production of fresh water and electricity via multistage solar photovoltaic membrane distillation. *Nat. Commun.* **2019**, *10* (1), 3012.

(26) Tao, P.; Ni, G.; Song, C.; Shang, W.; Wu, J.; Zhu, J.; Chen, G.; Deng, T. Solar-driven interfacial evaporation. *Nat. Energy* **2018**, *3* (12), 1031−1041.

(27) Zhu, L.; Gao, M.; Peh, C. K. N.; Ho, G. W. Recent progress in solar-driven interfacial water evaporation: Advanced designs and applications. *Nano Energy* **2019**, *57*, 507−518.

(28) Liang, Y.; Ye, J.; Luo, X.; Chen, J.; Yang, Z.; He, J.; Chen, Y. Decoding the performance of module-scale interfacial desalination from a thermodynamic perspective. *Desalination* **2023**, *565*, 116818.

(29) Xu, K.; Wang, C.; Li, Z.; Wu, S.; Wang, J. Salt mitigation strategies of solar-driven interfacial desalination. *Adv. Funct. Mater.* **2021**, *31* (8), 2007855.
(30) Du, C.; Zhao, X.; Qian, X.; Huang, C.; Yang, R. Heat-localized solar evaporation: Transport processes and applications. *Nano Energy* **2023**, *107*, 108086.
(31) Dang, C.; Wang, H.; Cao, Y.; Shen, J.; Zhang, J.; Lv, L.; Xu, G.; Zhu, M. Ultra salt-resistant solar desalination system via large-scale easy assembly of microstructural units. *Energy Environ. Sci.* **2022**, *15* (12), 5405−5414.
(32) Chen, C.; Kuang, Y.; Hu, L. Challenges and opportunities for solar evaporation. *Joule* **2019**, *3* (3), 683−718.
(33) Zhang, Y.; Xiong, T.; Nandakumar, D. K.; Tan, S. C. Structure architecting for salt-rejecting solar interfacial desalination to achieve high-performance evaporation with in situ energy generation. *Adv. Sci.* **2020**, *7* (9), 1903478.
(34) Liu, G.; Chen, T.; Xu, J.; Yao, G.; Xie, J.; Cheng, Y.; Miao, Z.; Wang, K. Salt-rejecting solar interfacial evaporation. *Cell Rep. Phys. Sci.* **2021**, *2* (1), 100310.
(35) He, W.; Zhou, L.; Wang, M.; Cao, Y.; Chen, X.; Hou, X. Structure development of carbon-based solar-driven water evaporation systems. *Sci. Bull.* **2021**, *66* (14), 1472−1483.
(36) Zheng, Z.; Liu, H.; Wu, D.; Wang, X. Polyimide/MXene hybrid aerogel-based phase-change composites for solar-driven seawater desalination. *Chem. Eng. J.* **2022**, *440*, 135862.
(37) He, W.; Zhou, L.; Wang, Y.; Yu, L.; Hou, Y.; Bi, S.; Wang, M.; Hou, X. Ternary hierarchical structure based solar-driven evaporator for long-lasting concentrated brine treatment. *EcoMat* **2023**, *5*, No. e12355.
(38) Wilson, H. M.; Suh, Y.; Lim, H. W.; Raheman AR, S.; Lee, S. J. A low-cost plant transpiration inspired 3D popsicle design for highly efficient solar desalination. *Desalination* **2023**, *563*, 116731.
(39) Lian, P.; Yan, R.; Wu, Z.; Wang, Z.; Chen, Y.; Zhang, L.; Sheng, X. Thermal performance of novel form-stable disodium hydrogen phosphate dodecahydrate-based composite phase change materials for building thermal energy storage. *Adv. Compos. Hybrid Mater.* **2023**, *6* (2), 74.
(40) Stroock, A. D.; Pagay, V. V.; Zwieniecki, M. A.; Michele Holbrook, N. The physicochemical hydrodynamics of vascular plants. *Annu. Rev. Fluid. Mech.* **2014**, *46*, 615−642.
(41) Tyree, M. T. Plant hydraulics: the ascent of water. *Nature* **2003**, *423* (6943), 923.
(42) Duan, C.; Karnik, R.; Lu, M.-C.; Majumdar, A. Evaporation-induced cavitation in nanofluidic channels. *Proc. Natl. Acad. Sci. U.S.A.* **2012**, *109* (10), 3688−3693.
(43) Sperry, J. S.; Tyree, M. T. Mechanism of Water Stress-Induced Xylem Embolism. *Plant Physiol.* **1988**, *88* (3), 581−587.
(44) Tas, N. R.; Mela, P.; Kramer, T.; Berenschot, J. W.; van den Berg, A. Capillarity induced negative pressure of water plugs in nanochannels. *Nano Lett.* **2003**, *3* (11), 1537−1540.
(45) Caupin, F.; Herbert, E. Cavitation in water: a review. *C. R. Phys.* **2006**, *7* (9−10), 1000−1017.
(46) Mi, B.; Finnerty, C.; Conway, K. Prospects of artificial tree for solar desalination. *Curr. Opin. Chem. Eng.* **2019**, *25*, 18−25.

https://doi.org/10.1021/acs.est.3c08848
Environ. Sci. Technol. 2024, 58, 3800−3811